Journal of Building Engineering 28 (2020) 101100

Contents lists available at ScienceDirect

Journal of Building Engineering

journal homepage: http://www.elsevier.com/locate/jobe

Fragility of masonry veneers to human-induced Central U.S. earthquakes using neural network models

Farid Khosravikia [a,*], Jennifer Kurkowski [b], Patricia Clayton [a]

[a] Dept. of Civil, Architectural and Environmental Engineering, The University of Texas at Austin, Austin, Texas, USA
[b] Protective Design & Security, Thornton Tomasetti, Washington, DC, USA

ARTICLE INFO

Keywords:
Induce seismic hazard
Masonry veneers
Fragility assessment
Artificial neural network

ABSTRACT

Since 2008, an increase in human-induced seismic activity related to natural gas production and petroleum activities has resulted in millions of dollars of damage in the Central United States, primarily to residential buildings including chimneys and masonry veneers. This study aims to better understand and evaluate the impacts of such seismic hazards on masonry veneers. To do so, a probabilistic framework is proposed in which fragility curves representing the probability of cracking and collapse damage states for masonry veneers are developed. In the proposed framework, Artificial Neural Networks are adopted to develop probabilistic seismic demand models from experimentally-validated finite element analyses of non-seismically detailed masonry veneers. The framework utilizes a suite of 200 ground motions largely believed to be from human-induced earthquakes with magnitudes of 3.6–5.8 recorded in the Central U.S. since 2008. Fragility curves are produced for masonry veneers with code compliant corrugated brick ties and those with thinner brick ties that are commonly employed in residential construction in the Central U.S. Additionally, the proposed fragilities developed for human-induced earthquakes are compared to those from the literature, which were developed for the New Madrid seismic hazard and are commonly used for seismic vulnerability assessments of infrastructure in the Central U.S. The results indicate that for a given PGA level, induced earthquakes may be more likely to produce damage compared to earthquakes representing the New Madrid hazard. Finally, the regional extents of damage from a recent induced seismic event are estimated using the newly developed and existing fragility functions to evaluate the implications of using these models for regional vulnerability assessments.

1. Introduction and motivation

In 2016 alone, over 500 M3+ earthquakes have occurred in the Central United States, while in 1973–2008 there were only an average of 21 per year [1]. Such earthquakes, which have mainly occurred in the states of Oklahoma, Texas, and Kansas, are believed to be human-induced, associated with activities from the oil and gas industry [2–5]. For example, Ellsworth et al. [6] demonstrated that the increase in seismicity is inconsistent with natural processes in such a geologically stable region. It has also been shown that deep disposal of wastewater, which is the byproduct of oil and gas production, is the main contributor to the seismicity increase in these regions [7]. In 2017, these induced earthquakes occurred over broader areas than they had in previous years. Few of the 7 million people impacted by these events have previously dealt with the threat of earthquakes [8]. Although there has been a reduction in the rate of these earthquakes since 2018 compared to previous years, the number of earthquakes in this region is still much more than the expected rate from natural earthquakes.

According to the one-year USGS [8] earthquake hazard predictions accounting for induced seismic activity, the likelihood of experiencing minor damage from an earthquake in parts of the Central U.S., such as Oklahoma, is now comparable with that in California. Much of the observed damage following the 2011 M5.7 Prague, OK, the 2016 M5.8 Pawnee, OK, and the 2016 M5.0 Cushing, OK earthquakes mainly included masonry veneer and chimney failures in residential homes (examples shown in Fig. 1). This damage caused millions of dollars of insurance claims although only approximately 15% of properties in that area contain some level of earthquake insurance [9, 10]. Unlike areas of the West Coast where construction practices have changed with improved knowledge of seismic effects, these areas are most at risk to experience damage, particularly nonstructural damage, in existing buildings, which were designed with little to no consideration of

* Corresponding author. Tel.: +1 512 662 24782.
E-mail addresses: farid.khosravikia@utexas.edu (F. Khosravikia), JKurkowski@ThorntonTomasetti.com (J. Kurkowski), clayton@utexas.edu (P. Clayton).

https://doi.org/10.1016/j.jobe.2019.101100
Received 1 June 2019; Received in revised form 27 November 2019; Accepted 29 November 2019
Available online 30 November 2019

earthquake activity.

In addition, national building code committees are unsure of how to treat this new form of hazard, largely due to lack of information and uncertainty associated with predicting the magnitude and location of hazards tied to future human activity.

This paper investigates the fragility of modern residential construction, and more specifically non-seismically detailed masonry veneers in single-story wood-framed structures, to induced earthquake hazards. It is worth noting that the impacts of such earthquakes on chimneys are being studied in other ongoing research at University of Colorado Boulder [13,14]. While brick cladding, which is known to perform poorly during earthquakes, is less commonly used in modern construction in historically seismically active regions such as the West Coast of the U.S., areas with more recent increases in seismicity, such as Oklahoma, Texas, and Kansas, consist of a large population of brick clad homes that may be susceptible to seismic damage. In fact, census data from the West South Central subregion of the U.S., which includes Texas, Oklahoma, Arkansas, and Louisiana, indicates that over 60% of single-family homes constructed in this region in the years 1999–2012 had brick as the exterior material [15]. Damage to brick facades can cause physical hazards associated with the falling bricks, as well as the need for repairs that can become costly for building owners. The historical prevalence of residential buildings with brick masonry exteriors in areas of Texas and Oklahoma, where the increase in seismic activity has also been experienced, motivates the need to investigate their potential for seismic damage.

The vulnerability of masonry veneers is investigated within a probabilistic framework in which fragility curves are developed to estimate the likelihood of cracking and collapse damage states given Peak Ground Acceleration (PGA). In the framework, Artificial Neural Network (ANN) is utilized to develop the probabilistic seismic demand models based on response data from experimentally-validated finite element models. ANN [16–18] is a statistical method for function approximation to represent the underlying linear and nonlinear relations existing in a dataset. The advantages of using ANN models instead of conventional methods of developing seismic demand models (i.e. power functions, which are derived from linear regressions in the log-log space) are discussed in detail. The computational models used to predict the seismic response of the non-seismically detailed masonry veneers, considering different brick tie types, are described and compared to existing experimental data from the literature. The proposed framework also takes into account the uncertainty in ground motion selection considering a database of 200 ground motions from earthquakes classified as human-induced in the Central U.S.; see Section 3 for details.

The fragility of the masonry veneers subjected to induced seismic hazards are then compared with Modified Mercalli Intensity (MMI) [19] measures to investigate whether the damage caused by this type of seismic hazard is consistent with what is expected from Modified Mercalli Intensity damage descriptions. The fragility curves are also compared with existing fragility curves in the literature for non-seismically detailed masonry veneers. These existing fragility curves were developed based on the New Madrid seismic hazard, which has historically been used to evaluate seismic vulnerability in Central United States. The fragility curves are then combined with intensity contours from an induced earthquake event provided by ShakeMap [20] to evaluate and compare the regional damage estimates resulting from the use of new and existing fragility curves. ShakeMap is a product of the USGS Earthquake Hazards Program, which provides near-real-time maps and contours of shaking intensity following the earthquakes.

2. Proposed probabilistic framework

This study utilizes a probabilistic framework, which considers uncertainty in ground motions and local soil conditions, to develop fragility functions to evaluate the vulnerability of masonry veneers in Central United States. A fragility function provides the conditional probability of a structure meeting or exceeding a pre-defined level of damage (i.e., cracking and collapse) given a ground motion intensity. Here, Peak Ground Acceleration (PGA) is considered as the intensity measure (IM) of interest. For each damage state in the proposed framework, the probability of the damage, p_f, is the probability that the structural demand, D, meets or exceeds the structural capacity, C, which reads:

$$p_f = P[D/C \geq 1 \mid \mathrm{IM}] \quad (1)$$

The above-mentioned probability is estimated following the main steps shown in Fig. 2. As seen, to consider the uncertainty in the ground motion, the first step is to obtain a suite of ground motions that represent

Fig. 1. Damage to masonry-clad buildings due to Oklahoma earthquakes: (a) M5.0 Cushing [11], (b) M5.8 Pawnee [11], and (c) M5.7 Prague [12].

the seismicity of interest. Second, experimentally-validated numerical models are developed to simulate the seismic performance of the masonry veneers subjected to the suite of ground motions. For each ground motion-veneer pair, a nonlinear response history analysis is conducted to estimate the demands (d_i) of the masonry veneers given the IMs of the ground motions. To estimate the seismic response of the masonry veneers for different range of IMs, the ground motions are scaled to PGA levels ranging from 0.1 g to 1.5 g, with increments of 0.2 g. Note that the maximum magnitude of the induced earthquakes recorded so far is 5.8 associated with Pawnee, Oklahoma earthquake in 2016. For such an earthquake, the region-specific ground motion models such as Khosravikia et al. [21] and Zalachoris and Rathje [22], with 90% confidence, estimate that the PGA values nearby epicenter (i.e. at hypocentral distances, R_{hyp}, of 5 km) will vary between 0.2 g to 1.5 g. Thus, the ground motions are scaled up to PGA of 1.5 g to estimate damage at these larger shaking intensities. The impact of scaling factor on the conclusions derived throughout the paper will be discussed later in the paper.

Then, ANN-based probabilistic seismic demand models (PSDMs) are trained and developed using the pairs of IM-d_i from the nonlinear response history analyses to estimate the demands given the IMs. In addition, the probabilistic seismic capacity model (PSCM) is developed for individual veneer components based on results from past experimental tests to predict the capacity of the masonry veneers. Having both PSDM and PSCM for each component, Monto Carlo Simulation is conducted to develop the fragility curves. Each step of this numerical fragility procedure is described in detail in the following sections.

3. Ground motion database

To properly represent the induced seismicity in the Central U.S., 200 ground motions [23] from 36 different seismic events recorded in Oklahoma, Texas, and Kansas since 2008, are considered in this study. Literature has classified these earthquakes as human-induced earthquakes associated with natural gas and petroleum productions in that region [1,2]. Moreover, Khosravikia et al. [23] showed that the response spectra of the selected unscaled recordings compared well with the response spectra estimated based on USGS 1-year hazard maps for induced earthquakes in this particular region of Central United States. Fig. 3 shows the magnitude-distance distributions for the induced earthquakes considered in this study. The magnitudes of these records are between 3.6 and 5.8, with a maximum PGA of 0.6 g, recorded during the 2016 M5.0 Cushing, Oklahoma event. In addition, the depth of these earthquakes varies from 2.4 km to 14.2 km with a mean depth of 5.5 km, which indicates that most of them are shallow-depth compared to typical natural events; see elsewhere for details [21,22,24].

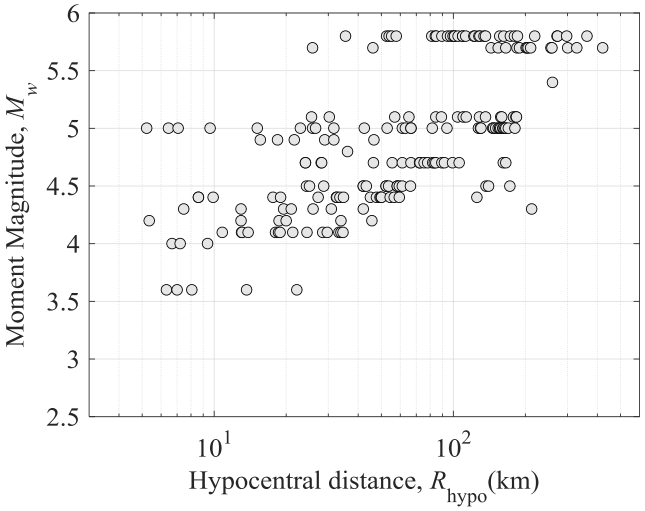

Fig. 3. Magnitude–distance distribution of induced ground motions in the Central U.S.

The 5%-damped elastic pseudo-acceleration spectra, S_a, of the selected records normalized with respect to their PGA, together with the overall mean, are shown in Fig. 4a. To compare the frequency content of the ground motions with those representing the New Madrid seismic hazard, Fig. 4b shows the S_a of the Wen and Wu ground motions [25] normalized with respect to their PGA. The Wen and Wu [25] ground motion database has been used in many studies to evaluate the seismic vulnerability of different types of infrastructure in the Central United States. The database contains 60 synthetic ground motion records representing earthquakes with magnitude of 5–8 in three cities in the Central U.S., namely Memphis, Tennessee; Carbondale, Illinois; and St. Louis, Missouri. As seen, for lower periods ($T < 0.25$s), the induced events, on average, have relatively larger normalized values of S_a compared to the Wen and Wu ground motions. However, spectral accelerations of the induced earthquakes diminish very quickly as the period increases. In fact, the energy concentration for induced earthquakes is mainly in the shorter period range from 0.1 to 0.3 s. This significant reduction in spectral acceleration at longer periods primarily relates to the relatively lower magnitudes of the induced earthquakes, which are not able to produce as much energy for long period waves.

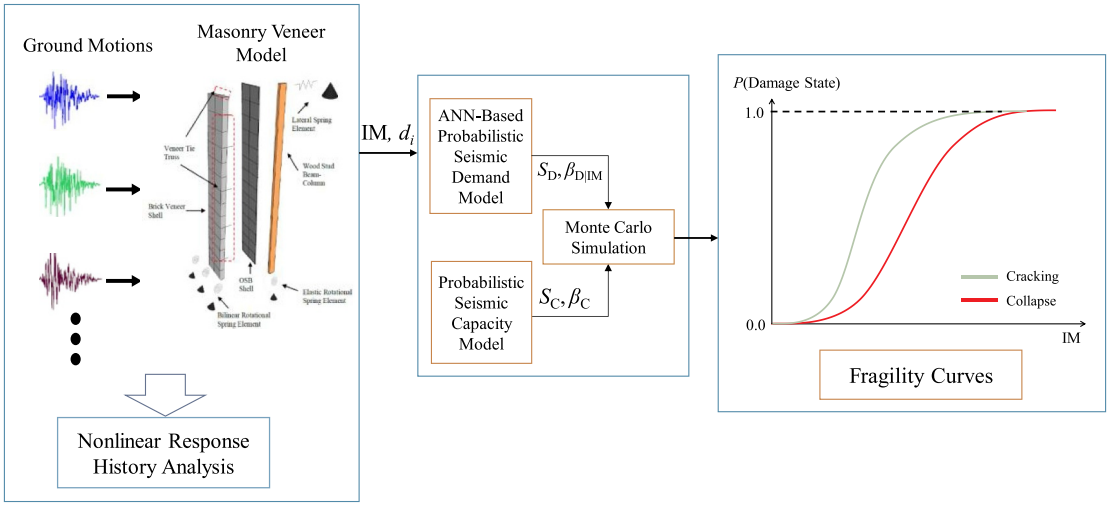

Fig. 2. Probabilistic framework for seismic vulnerability assessment of masonry veneers.

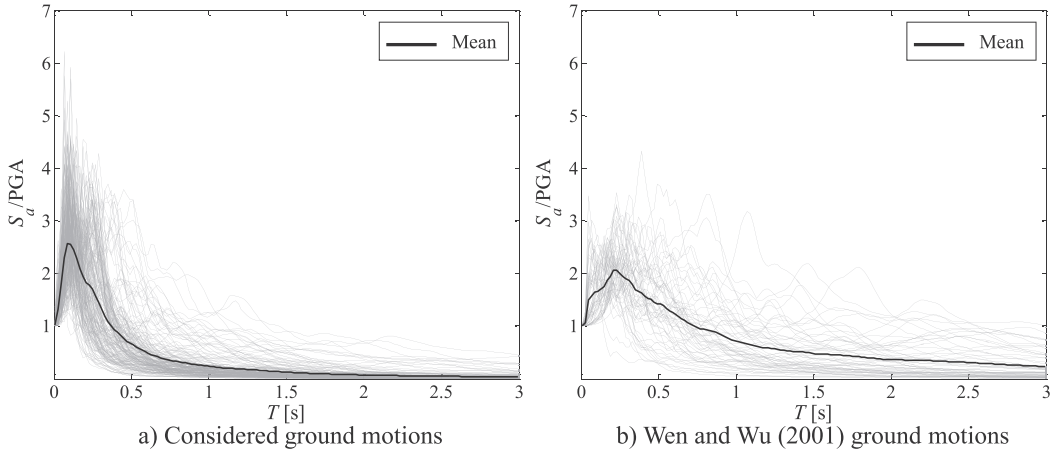

Fig. 4. Response spectra of ground motions normalized with respect to their PGA.

4. Numerical models and validation of masonry veneers

Fig. 5a and Fig. 5b shows a schematic view of the brick veneer wall considered in this study. In typical brick veneer construction, the brick façade is not load bearing, but rather is connected to the load bearing wall with veneer ties. The actual load bearing wall is often constructed of wood studs and oriented strand board (OSB), which are commonly employed in residential construction, or concrete masonry unit (CMU) blocks, which are more common in commercial buildings. Corrugated metal ties are one of the most common methods of veneer anchorage used in residential construction in low-seismic areas.

The behavior of the considered masonry veneers is simulated in the OpenSees analysis framework [26]. The software provides robust nonlinear dynamic analysis capabilities with numerous built-in and user-defined materials to represent a wide range of nonlinear behaviors. The developed OpenSees model, which is schematically shown in Fig. 5c, is based on the modeling approaches recommended by Reneckis and LaFave [27,34], hereafter referred to as R&L, with slight modifications. The numerical model is also validated using experimental data from the same study.

As seen in Fig. 5c, the behavior of a full wall panel is simulated by a wall strip model to increase computational efficiency when executing hundreds of nonlinear response history analyses. The strip model represents a 406 mm (16 inch) width of wall tributary to a single stud. With a 406 mm (16 inch) spacing between studs, the brick ties are typically spaced at 406 mm (16 inch) horizontally and 610 mm (24 inch) vertically to meet the prescriptive code required maximum tributary area of 248051 mm^2 (2.67 ft^2) per tie [28].

It is worth noting that the present study only considers out-of-plane shaking behavior of the masonry veneers as much of the observed damage to veneers was out of plane [29–32]. Moreover, variations in architecture like window openings and gables are not considered in the proposed strip models, which are only meant to simulate full wall panels. Page [33] showed that such variations in architecture could make masonry veneers even more vulnerable to damage. Additionally, the strip model does not consider corner effects in buildings where the continuity of the masonry veneers along a perpendicular wall may have some localized effects on performance. In the following sections, the modeling of each component of the brick veneers, including the ties, the bricks, the 2 × 4 studs, and the OSB panels are discussed separately.

4.1. Numerical models

It has been found that the overall veneer wall performance due to out-of-plane shaking directly correlated to the tie tensile properties, indicating the importance of focusing on the installation and characteristics of the ties when trying to evaluate performance of the veneer wall [27,32,34,35]. The previous R&L study considered various corrugated brick tie thickness and fastener placement combinations in their study. This study included monotonic and cyclic tests of tie

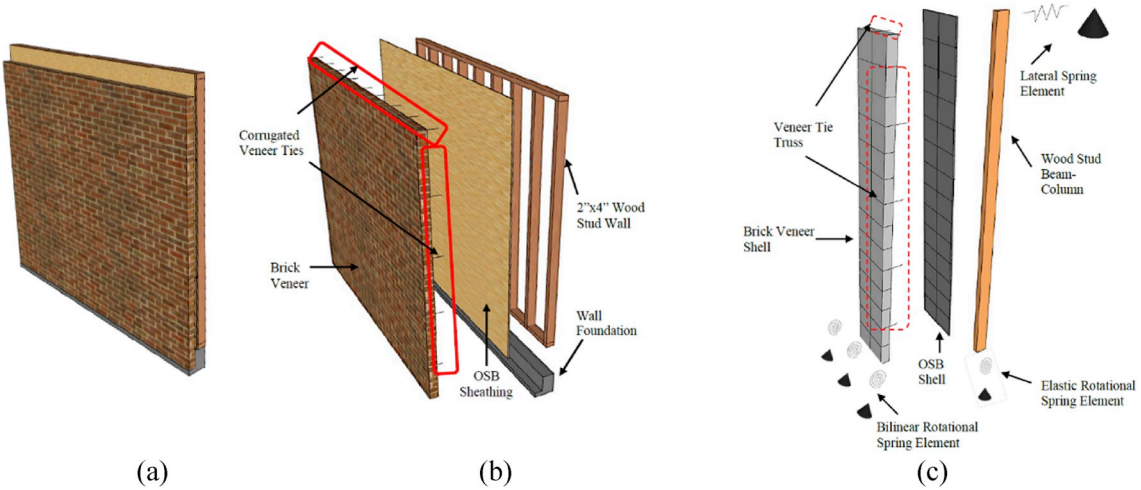

Fig. 5. Renderings of brick veneer wall: (a) Actual wall panel as constructed, (b) Actual wall with individual elements labeled, (c) Schematic view of veneer strip model developed in OpenSees.

subassemblies, as well as shake table tests of two full-scale wall panels typical of Central U.S. construction subjected to ground motions of increasing intensity, each with different brick tie types and fastener locations. In this study, the tie subassembly tests are used to inform modeling of the tie behavior, and the wall panel shake table tests are used to validate the wall strip model behavior.

In the present study, two types of corrugated brick ties, corresponding to those investigated in the R&L shake table study, are considered as: (1) ties with the minimum code-required thickness of 0.644 mm (22-gauge) with an 8d nail fastener located at the maximum code allowable installation eccentricity, 12.7 mm (½ inches), hereafter referred to as code-compliant brick ties (22ga-ecc), and (2) ties with thickness of 0.321 mm (28-gauge) that are thinner than code requirements [28] with an 8d nail fastener located at the minimum code allowable installation eccentricity, 4.0 mm (5/32 inches), hereafter referred to as thinner brick ties (28ga-min). While not code compliant, the 28-gauge ties are commonly used on residential construction sites in the Central U.S., mainly due to lack of code adoption or stringent code enforcement in the residential building sector, as indicated from personal conversations with anchorage suppliers, (C. Bupp, personal communication, July, 2017; P. Curtis, personal communication, July, 2017), and engineers from a forensic engineering firm in the region (R. Chamra, personal communication, March, 2017). Moreover, although in a different context, LaFave et al. [36] found that many of the brick veneers on residential homes that were damaged during the 2013 tornadoes in Oklahoma did not meet code requirements for connecting the veneer to the back-up structure, including the use of 28-gauge ties.

In this study, the brick ties, which are the primary source of nonlinearity in the brick veneer system and typically govern veneer out-of-plane performance, are modeled using nonlinear uniaxial truss elements. Uniaxial hysteretic materials are defined for each tie type. Fig. 6 shows the proposed backbones employed in OpenSees, the backbone models proposed from R&L, as well as the average backbone from 11 cyclic tie subassembly tests conducted by R&L for each tie type. As seen, the proposed OpenSees backbone is similar to what is suggested by R&L. The slight deviation between the proposed backbones and those of R&L is primarily to achieve more accuracy in matching the wall responses of the OpenSees models with those from the experiments, as will be presented later. According to R&L, tie performance is evaluated by its deformation. In fact, it is assumed that a tie fails when its deformation reaches the deformation at the peak strength. Thus, according to the proposed backbones shown in Fig. 6, tie failure occurs when its deformations reaches 6.85 mm (0.27 in) and 4.32 mm (0.17 in) for code-compliant (22ga-ecc) and thinner (28ga-min) brick ties, respectively. As was done by R&L, the behavior of the veneer models will be evaluated considering the strength degrading behavior following the tie failure deformation, as well as considering a brittle failure after tie deformation to see which failure model best matches the wall panel tests.

For the purposes of demonstration, cyclic behavior of an individual tie subassembly is demonstrated in Fig. 7 for the code-compliant (22ga-ecc) brick tie type. The figure shows the cyclic behavior of the tie before and after the tie failure point. Here, the hysteretic behavior is captured by the *Hysteretic* material available in OpenSees with pinching parameters of 0.85 and 0.3 in x- and y-directions, respectively. The subassembly testing focused on loading the ties cyclically in tension. Compression response of the ties is ignored, as it is assumed that mortar droppings behind the wall would provide a direct compressive load path from the brick veneer to the backing structure. Thus, the tensile tie behaviors described above are combined in parallel with an elastic-no-tension material with a very stiff response in compression in the OpenSees model.

Second, the brick veneer and the OSB sheathing, shown in Fig. 5c, are modeled using Shell elements with the properties shown in Table 1. These values are based on typical values for standard "Colonial Red" bricks, Type N mortar, and typical OSB sheathing, and they are the same as those used in R&L. For simplicity, the present study, similar to R&L, assumes that the shell elements remain elastic, and out-of-plane nonlinearity in the wall is concentrated in the brick ties and rotational spring at the base of the wall. Note that for this study, the primary indicator of damage, specifically veneer cracking and impending collapse, is correlated to tie failure, as was observed by R&L in the wall panel shake table tests. Following tie failure, nonlinear behavior is observed in the brick and mortar joints as the brick wall collapses out-of-plane; however, this nonlinearity was not explicitly modeled as it occurs after the tie failure-related damage states of interest in this study.

The wood 2 × 4 studs are modeled using elastic beam-column elements in OpenSees. The material properties, which were determined from the *National Design Specification for Wood Construction* [37], and experimentally measured weights are shown in Table 1. The shear modulus (G) of 4598 Mpa (667 ksi) is also considered for wood. Moments of inertia are determined from the cross-section of a 2 × 4 wood stud. In addition, as shown in the rendering of the real veneer wall in Fig. 5b, horizontal 2 × 4 top and sole plates are placed at the top and bottom, respectively, of the vertically oriented studs to complete the stud wall subassembly and provide stability. Therefore, the model also includes a horizontal wood beam-column element at the top and bottom of the vertical stud in the strip model. The horizontal 2 × 4 elements contain the same material and cross-section properties as those of the vertical stud.

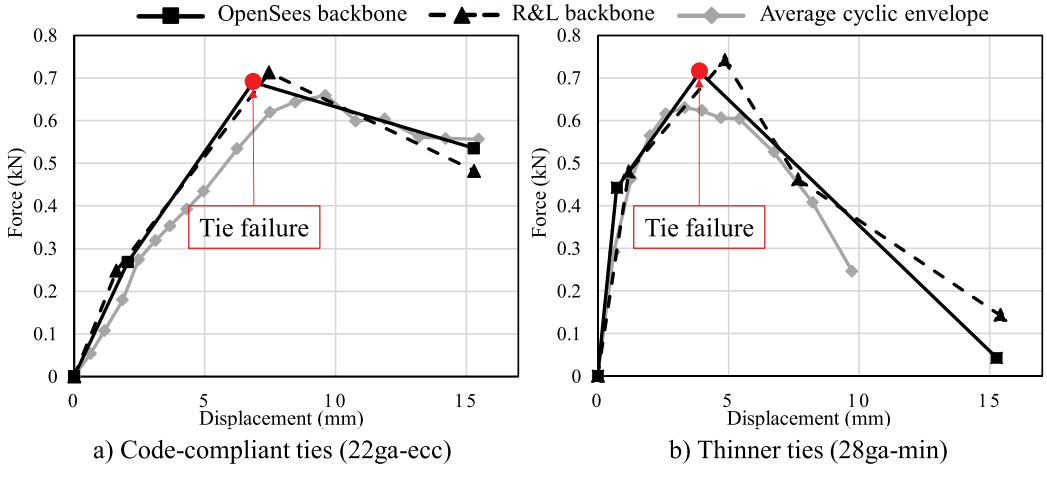

Fig. 6. Hysteretic backbones for different brick ties.

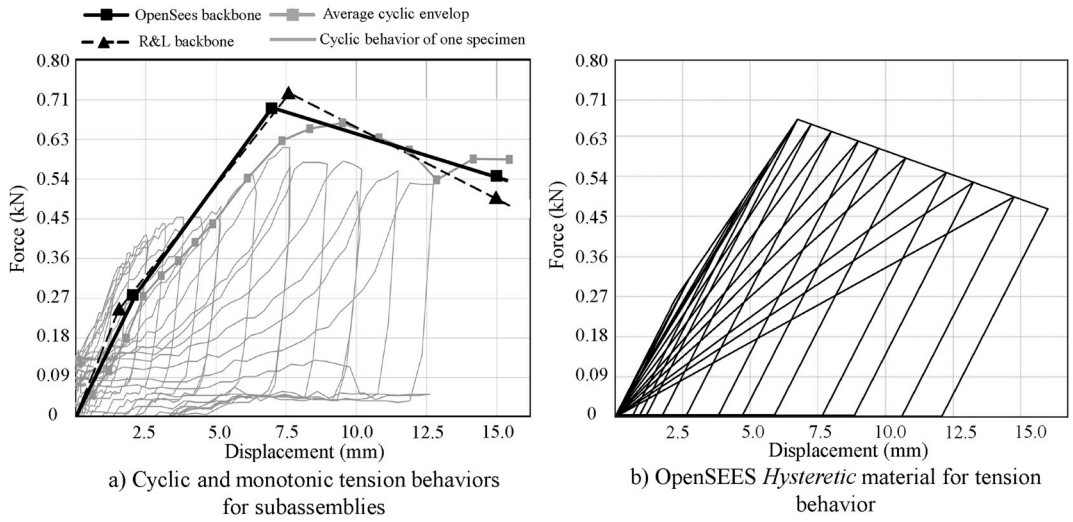

Fig. 7. Cyclic behavior of tie subassemblies and OpenSees hysteretic material for code-compliant brick ties (22ga-ecc).

Table 1
Material Properties of the veneer model.

Component	Elastic Modulus, E (MPa)	Poisson's Ratio, ν	Density, ρ (kg/m^3)	Thickness (mm)
Brick Veneer	13790	0.2	1842	89
OSB Sheathing	6412	0.4	1160	11
Wood Stud	8274	0.4	420	N/A

As shown in Fig. 5c, the stud boundary conditions include a pinned out-of-plane lateral spring at the top of the stud assembly to simulate the lateral resistance provided by the rest of the structure, as well as a pinned rotational spring at the bottom of each stud and veneer to simulation rocking behavior at the base of the wall. Translational degrees of freedom at the base of the brick veneer and stud wall are restrained. The lateral restraint spring representing the connection of the stud wall to the rest of the structure, is assumed to behave elastically in this model, which is consistent with lack of structural damage observed in recent earthquake events in Oklahoma, shown in Fig. 1. The stiffness of the lateral restraint spring is computed as 303.5 kN/m (1.7 k/in), which is determined by comparing static load test displacements from the model to those observed in the experimental tests. In addition, similar to Doherty et al. [38] and Simsir [39], bilinear rotational springs, with nonlinear behaviors defined based on the veneer wall weight and geometry, are used at the base of the brick veneer to simulate rigid body rocking response of the brick as it pivots around its base. Fig. 8 shows the nonlinear behavior defined in the OpenSees. The M_{max} and θ_{max} are determined based on weight, height, and out-of-plane thickness of the brick veneer in the strip model [39] and are designated as 150 N-m (1330 l b.in) and 0.045 radians, respectively. The idealized rigid body rocking behavior would be simulated with an infinite initial stiffness up to M_{max} and following a downward slope to θ_{max}; however, as was done by R&L, to mitigate numerical convergence issues, a semi-rigid model based on recommendations from Doherty et al. [38] is used, where a reduced initial slope is used up to $\theta_{max}/9$, after which, the spring follows the downward slope from the idealized model, as shown in Fig. 8.

Unlike the brick veneer wall, the rigid body rocking behavior was observed not to be significant for the wood stud wall due to the tie downs provided to the foundation. Thus, elastic rotational springs supporting the studs are used to simulate the rotational restraint provided by the OSB fastened to the sole plate. According to R&L, a stiffness of 110 kN-m/rad (1000 k-in/rad), which is determined by comparing the displacements from static tests on the computational model to those measured from the experimental tests, is assigned for this spring.

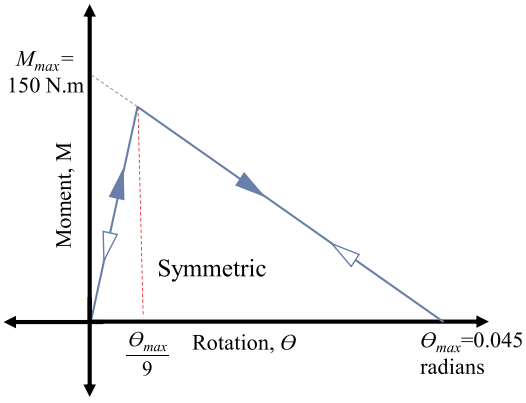

Fig. 8. Bilinear elastic rocking behavior model at the base of the brick wall. The blue arrows represent the loading behavior and the white represents the unloading behavior along the same path. (For interpretation of the references to colour in this figure legend, the reader is referred to the Web version of this article.)

Seismic masses are included for each element in the proposed OpenSees model by designating the material density (shown in Table 1) for each individual component in the model. The shell element mass is distributed based on the specified shell dimensions and shell material density. The nonlinear beam-column elements, used for wood studs, also utilize the material density to distribute mass along the height of the stud within OpenSees. An additional lumped mass is added to the top of the veneer where the top tie is located to account for the additional bricks in the top few rows of the veneer wall above the top tie. No additional gravity loads are applied to the model, as geometric nonlinearity is not considered in the analysis.

Finally, it should be noted that, as determined by R&L, a 4% damping ratio in the first and second modes was designated for Rayleigh damping for the nonlinear response history analyses. In the analysis, the earthquake excitation is applied to all support nodes in the out-of-plane direction. Fig. 9 shows the schematic view of the computational model with the defined dimensions and tie locations utilized for analysis.

4.2. Model validation

The tie backbones and cyclic behavior were validated using cyclic tie subassembly experimental data available in the literature, as discussed

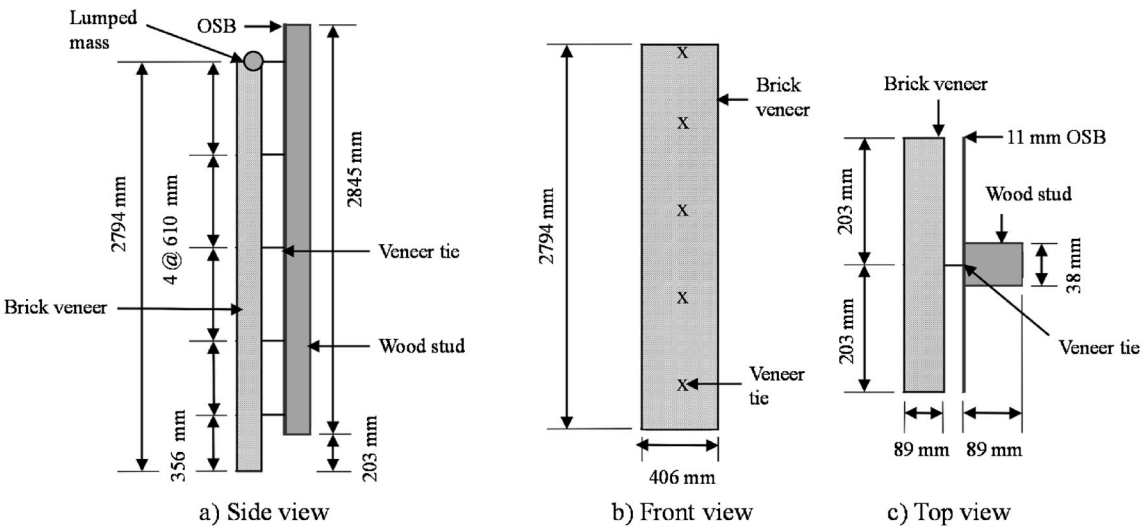

Fig. 9. Dimensions of computational model for masonry veneer.

in the previous section. This section discusses the validation of the entire strip model with dynamic out-of-plane shake table testing of full-scale wall panel specimens. To do so, response history analyses are conducted in OpenSees for the same ground motion used in the full-scale wall panel experiment, which is a synthetic 10% in 50-year event for Memphis, Tennessee, with a PGA of 0.059 g, from the Wen and Wu [25] ground motion set. The full-scale wall panels, which were similar to the one shown in Fig. 5a, employed the typical 406 mm-by-610 mm (16 inch-by-24 inch) tie spacing, with each wall employing one of the two predefined tie types. Each wall panel was subjected to multiple shaking events using the same earthquake ground motion scaled to increasing intensities with each test. Additional details of the wall panel specimens and shake table tests can be found in Reneckis and LaFave [27].

To validate the elastic behavior of the model, the strip models are subjected to shaking levels that would not result in tie damage, and the experimental displacements of the back-up structure and of the veneer at different heights at the middle of the wall panel are compared to those from the model. Fig. 10a and Fig. 10b demonstrate the results for wall panels with code-compliant (22ga-ecc) and thinner (28ga-min) brick tie types, respectively. The displacement results in the figure are from one ground motion response history, and the intention is to document the overall wall behavior in its elastic range, before failure of the top tie. Results from testing the wall with code-compliant brick ties in Fig. 10a are obtained by scaling the ground motion acceleration time history, with an original PGA of 0.059 g, up to a PGA of 0.38 g, and the results from the wall with thinner brick ties are obtained by scaling up to a PGA of 0.18 g. The displacement profiles in Fig. 10 are at the time where the top of the veneer reached its peak displacement. It should be noted that the wall panel with thinner (28ga-min) brick ties becomes unstable at lower PGAs than the panel with code-compliant (22ga-ecc) brick ties, so the displacement profiles are shown for a lower PGA level. As seen in the figure, the experimental and OpenSees models of the veneer walls show similar behavior up the height of each wall. The minor variations between the computational models and the actual wall specimens, in Fig. 10, can be attributed to the strip idealization of a full wall panel, as well as slight differences and uncertainty in real tie and veneer stiffness values.

Furthermore, Fig. 11a and Fig. 11b show the displacements at the top

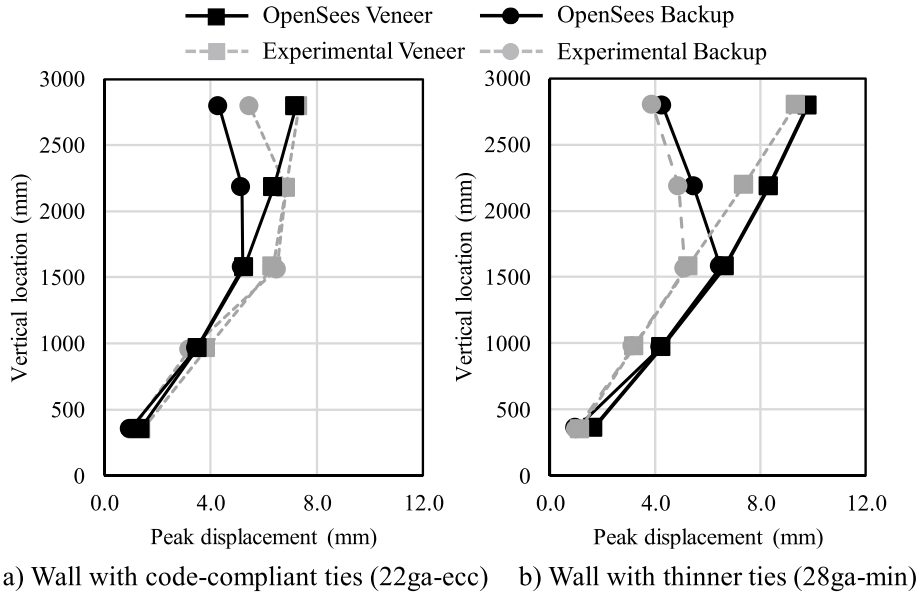

Fig. 10. Strip model validation: displacement profile along height of the wall panels.

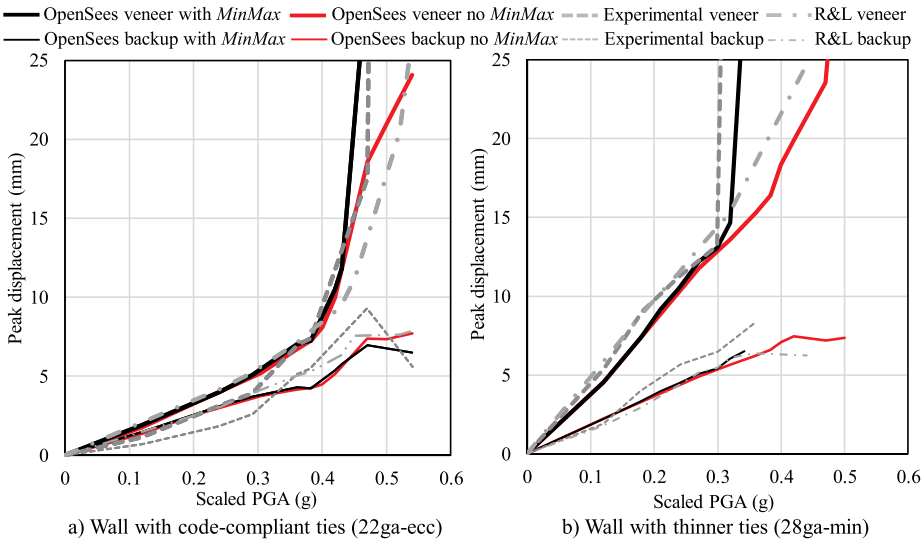

Fig. 11. Strip model validation: peak displacements versus PGA level.

of the brick veneer and at the top of the wood backup for different levels of shaking intensity for code-compliant (22ga-ecc) and thinner (28ga-min) brick tie types, respectively. Each plot compares the results from a series of shake table test conducted by R&L with the same wall panel subjected to a single ground motion scaled to increasing intensity levels, along with the results from the current OpenSees models, and those from the numerical models developed by R&L for reference.

Here, in the OpenSees model, two types of behavior are considered for veneer ties after reaching to the failure point. First, the cyclic strength deterioration observed in Fig. 7 are considered for veneer ties, and the behavior is shown by the red curves in Fig. 11a and b. Second, similar to R&L, it is assumed that the tie elements, in the model, provide no resistance once they exceed their peak strength to simulate brittle fracture (i.e. when they fail). In this case, the *MinMax* material in OpenSees is used to remove the tie elements from the numerical model. The results for this behavior are shown by the black curves in Fig. 11a and b. As seen in the figure, the latter approach results in a better match to the experimental results. Thus, the second approach, which is similar to the conclusion made in R&L, is considered for the post failure behavior of tie.

In this regard, the close correlation, shown in Fig. 11a and b, between the OpenSees models and the experimental wall behaviors and displacement values validate the veneer wall model as a whole. Moreover, the plots also show that the OpenSees model results are similar to, or in some cases better than, the R&L model results for predicting peak wall displacements.

5. Probabilistic seismic capacity model

For each veneer type, two damage states are defined as (i) repairable cracking damage and (ii) wall instability or collapse. Generally, out-of-plane brick veneer damage is directly correlated to the veneer tie deformation, because tie failure directly leads to veneer instability and separation from the backup system. Based on experimental observations and recommendations from R&L, repairable damage correlates with failure of the top row of ties, while wall instability or collapse typically occurs after failure of the top two rows of ties on a wall panel. As discussed in previous section, code-compliant (22ga-ecc) and thinner (28ga-min) brick tie are assumed to fail at deformations larger than 6.85 mm (0.27 in) and 4.32 mm (0.17 in), respectively, which, according to Fig. 6, represent the deformations at peak strength. Here, to account for the uncertainty in the tie capacity, it is assumed that the capacity for each limit state follows a lognormal distribution with a median of S_C, given as the previously stated deformation capacities, and dispersion of β_C. To determine the β_C, the coefficient of variation (COV) of 25% is taken into account, which results in β_C of 0.25 using the following equation:

$$\beta_C = \sqrt{\ln\left(1 + \mathrm{COV}^2\right)} \tag{2}$$

Table 2 shows the natural periods (T_n) of the veneer strip models before and after failure of the top tie, which is always the first tie to fail in a solid wall panel. The latter natural period is determined by removing the top tie from the model and recalculating the natural period, and hereafter is referred to as elongated period (T_m). Similar to R&L, the remaining undamaged ties are assumed to be in their elastic range when the top tie fails, so there is no reduction in stiffness for those ties for calculation of the natural period after the top tie failure. As expected, the natural periods of wall models increase as the wall is damaged and the stiffness of the system is decreased. Moreover, as seen in the table, veneers with the thinner (28ga-min) brick ties generally have longer natural periods compared to the model with the code-compliant (22ga-ecc) brick ties.

6. Probabilistic seismic demand model

Probabilistic seismic demand model (PSDM) predict the demand of the structure with respect to the ground motion IM based on the results from the nonlinear response history analyses. In this study, PSDMs are developed for the deformation of the top two ties, which are the seismic demands used to evaluate damage of the masonry veneers. Conventionally, it is assumed that the median of seismic demands, S_D, follows a power function of intensity measure as follows:

$$S_D = a\mathrm{IM}^b \tag{3}$$

This equation can be rearranged to logarithm space where $\ln(S_D)$ follows a linear function of ln(IM) with coefficients $\ln(a)$ and b. See, for instance, Cornell et al. [40], Nielson et al. [41], and Padgett et al. [42], among others. In such studies, coefficients a and b can be computed by fitting a linear regression to the lognormal of the outputs from nonlinear

Table 2
Natural period of the veneer model before and after top tie failure.

Brick tie type	Natural period, T_n	Elongated period, T_m
Code-compliant ties (22ga-ecc)	0.125 s	0.265 s
Thinner ties (28ga-min)	0.131 s	0.269 s

response history analyses. However, in reality, the relationship between the demands and IMs does not necessarily follow the predefined linear shape in natural log space. Thus, the present study adopts Artificial Neural Network (ANN) as the statistical method to extract more complex, nonlinear behaviors that inherently exist in the nonlinear response history data, which can lead to more accurate estimates of the median of the demand. It is worth noting that while ANN is used in this study, other machine learning algorithms, such as random forest and support vector machine, could also be used as an alternative to extract the nonlinear trends existing in the dataset.

ANN, which was developed by McCulloch and Pitts in the early 1940s [43], is a statistical learning model inspired by biological neural networks in the human brain. Fig. 12 shows a schematic view of the relatively simple ANN model considered in this study. Here, a multilayer perceptron network, which is a kind of ANN with a feed-forward architecture [44], is utilized. As seen in the figure, IM and structural demand are respectively set as the input and output of the model. Moreover, the ANN network consists of a hidden layer with two neurons. The size of the hidden layer is determined through a sensitivity analysis by training different ANN models considering different hidden layer sizes varying between 1 to 8 and evaluating their performance based on the mean square error. The sensitivity analysis showed that although there is a reduction in the mean square error as the number of neurons in the hidden layer increases, this reduction is minimal for hidden layer sizes larger than two. Moreover, use of more than four neurons, for this specific problem, where the demand is estimated by only one input parameter (i.e. IM), has the potential to cause overfitting. Overfitting is a modeling error that occurs when the model is too closely fit to a particular set of data, and may therefore fail to reliably predict future observations. Therefore, for simplicity, two neurons are considered in the hidden layer of the ANN models in this study.

The neurons of each layer are connected to the neurons of other layers with connection weights. In addition, a bias parameter is introduced to each neuron to provide flexibility to the ANN model by preventing the model from producing zero values for zero inputs. The output of each neuron is computed by passing the summation of the weighted inputs received by the neuron as well as the bias parameter through an activation function specified for each neuron of the model. The activation function provides the model with the ability to simulate the nonlinear behaviors that exist in the data. Here, a log-sigmoid function of $\phi(x) = \left(\frac{1}{1+e^{-x}}\right)$ and linear function of $\phi(x) = x$ are considered as the activation function of the neurons in the hidden and output layers, respectively. These are the two common activation functions used in engineering problems [45,46].

To compute the connection weights and bias terms, the network is trained using the Levenberg–Marquardt back-propagation algorithm [47], which is a standard nonlinear least squares optimization algorithm. In the training process, a regularization method [48] is implemented to prevent from overfitting. In this method, the data from the response history analyses are divided into two different subsets, training and testing subsets, which respectively consist of approximately 80% and 20% of the database. The training subset is used for determining the weights and bias values, and the testing subset is used to test the reliability of the model prediction for future data to ensure that the overfitting error does not exist in the model.

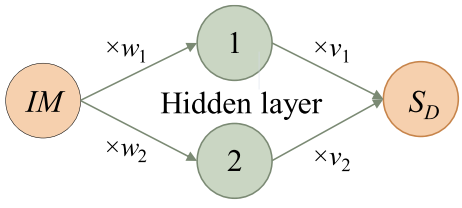

Fig. 12. ANN-based probabilistic seismic demand model.

After training, the ANN model shown in Fig. 12 can be written as a mathematical formulation as follows:

$$\ln(S_D) = b + \sum_{i=1}^{2} v_i \times \left[\frac{1}{1+\exp[-(w_i \times \ln(IM) + b_i)]}\right] \quad (4)$$

where w_i is the connection weights entering the i-th neuron of the hidden layer from the input neuron; b_i denotes the bias of the hidden layer neurons; b and v_i, respectively, represent the bias value and the connection weights for the output neuron. The connection weights and bias values are computed from the training process. As noted, the PSDMs, in this study, are trained for the top two tie deformations (d_1 and d_2, respectively) of the masonry veneers with respect to PGA. In this regard, Table 3 shows the values of the coefficients of the ANN-based PSDMs trained for masonry veneers with code-compliant (22ga-ecc) and thinner (28ga-min) brick ties. Using Eq. (4) and the coefficients presented Table 3, one can easily estimate the tie deformations given the PGA value of the ground motion without re-training the ANN models.

Moreover, similar to previous studies [40–42], the conditional seismic demands are assumed to follow a lognormal distribution, resulting in normal distribution with median of $\ln(S_D)$ and dispersion of $\beta_{D|IM}$ in the transformed space. The variation or dispersion of the seismic demands about the mean given the intensity measure is the conditional lognormal standard deviation of the seismic demand ($\beta_{D|IM}$). Similar to Padgett et al. [42], $\beta_{D|IM}$ is here estimated by computing the dispersion of the data around the values predicted by the statistical model using the following equation:

$$\beta_{D|IM} = \sqrt{\frac{\sum_{i=1}^{N}[\ln(p_i) - \ln(S_D)]^2}{N-2}} \quad (5)$$

where p_i is the peak demand of the tie of interest and N is the number of response history analyses conducted for the masonry veneers. Table 3 shows the value of $\beta_{D|IM}$ for the ANN-based PSDMs developed for estimating top two tie deformations of masonry veneers with respect to PGA.

6.1. Comparison of ANN-Based PSDMs with conventional linear models

To compare the predictive power of conventional linear regression (Eq. (3)) and ANN-based (Eq. (4)) models, Fig. 13a depicts the demands and median values derived from linear regression and ANN models versus PGA of the ground motions in natural log space. For the purpose of demonstration, the results are shown for top tie deformation of code-compliant (22ga-ecc) masonry veneers. As seen in the figure, the demand does not follow a linear function with respect to the PGA in natural log space. For some of the response history analyses at larger intensity levels, there is an increase in the structural demands, which stems from the loss of strength in the ties after they reach their peak strength. As seen in the figure, ANN is able to properly capture the trends observed in the data and provides more accurate estimates of the median structural demand. The linear model, however, overestimates the median demand for lower values of PGA and tends to underestimate the demands for larger values.

Moreover, Fig. 13b shows the correlation between the predicted value of the demand from ANN and linear model against the measured value from the response history analyses. The dashed line in the plot indicates the ideal case where the predicted values equal the measured values. As seen in the figure, the data from ANN is closer to the ideal line, indicating a stronger correlation between the estimated and measured values. To quantify this correlation, the Pearson Correlation Coefficient, R, between the predicted and measured values is computed for both statistical models, and the results are shown in Fig. 13b. R varies between 0 to 1 representing no to full correlation, respectively. This

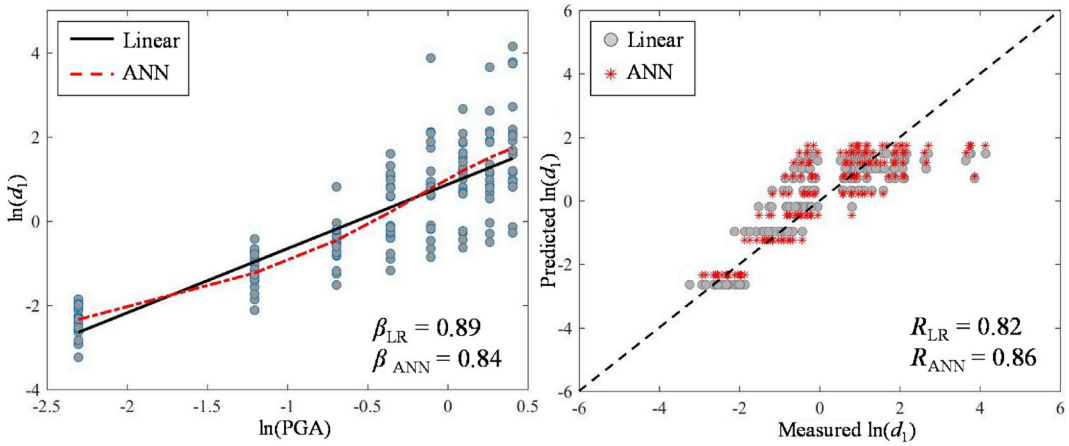

(a) Top tie deformation versus PGA (b) Predicted versus measured values

Fig. 13. Comparison of the ANN-based and linear-based PSDMs for the top tie in a veneer model with code-compliant ties (22ga-ecc). R_{LR} and β_{LR} respectively show the correlation coefficient, R, and standard deviation, $\beta_{D|IM}$, from linear regression, while R_{ANN} and β_{ANN} show those from ANN model.

parameter is used in many studies to evaluate the predictive power of statistical models. See for example, Alavi and Gandomi [49], Liu et al. [50], Gandomi et al. [51], Tokunaga et al. [52], Gandomi et al. [53], and Khosravikia and Clayton [54], among many others. As seen in the figure, the larger R value for ANN indicates that the model provides stronger correlation between the estimated and the measured values. Finally, the estimated standard deviation, $\beta_{D|IM}$, is also shown in Fig. 13a for both methods. As seen, using ANN instead of a linear model reduces the uncertainty of the demand model, indicating more accurate estimates. Thus, ANN is used to develop the PSDMs in this study. For the cases where the data follow a linear trend in the transformed space, ANN and the linear model lead to very similar median value estimates.

7. Fragility of masonry veneers for Central United States

Given demand and capacity models, the probability of damage is computed using Monte Carlo simulation. In each sample of Monte Carlo simulation, random realizations are generated for the demand and capacity, and the damage is evaluated by comparing the paired realizations. To properly account for the uncertainty of demand and capacity, 10^6 number of realizations are generated for each specific value of the considered IM (i.e PGA in this study). Hence, probability of damage at a given PGA value is estimated as the number of samples that exceeded that limit state divided by the total number of samples, as indicated in Eq. (1). This sampling is then carried out over a wide range of PGA values to compute the probability of damage for different values of PGA, which forms the underlying data for the generation of fragility curves.

Fragility curves for the cracking and collapse damage states of masonry veneers with code-compliant (22ga-ecc) and thinner (28ga-min) brick ties are shown in Fig. 14. As seen in the figure, masonry veneers with thinner (28ga-min) brick ties are more vulnerable than those with code compliant (22ga-ecc) ties. For example, the median PGA for the cracking damage state is 0.36 g and 0.52 g for thinner (28ga-min) and code-compliant (22ga-ecc) brick ties, respectively. That is, for ground motions with PGA of 0.36 g and 0.52 g, there is 50% probability of exceeding cracking damage for wall panels with thinner (28ga-min) and code-compliant (22ga-ecc) ties. Moreover, according to Fig. 14, regardless of the masonry veneer tie type, the separation between the fragility functions for the collapse and cracking damage states are relatively small, indicating that after failure of the top tie, it is very likely that the second tie will fail when the wall is subjected to slightly larger accelerations.

For purposes of comparison, it should be noted that the largest PGA values recorded in the ground motions used in this study came from the

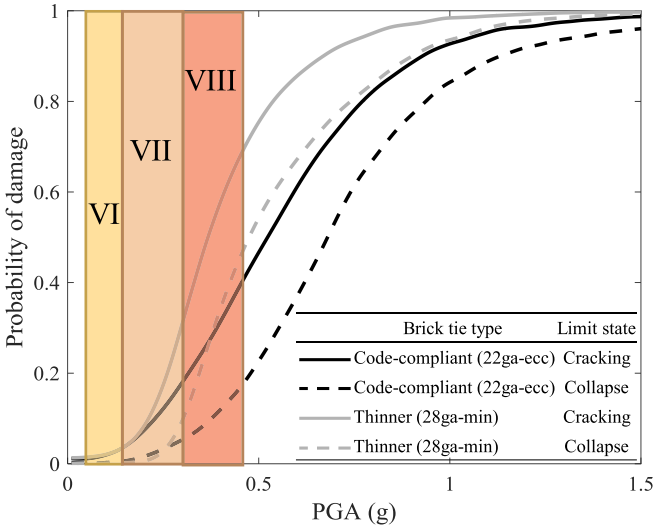

Fig. 14. Fragility curves for both masonry veneers with code-compliant (22ga-ecc) and thinner (28ga-min) brick ties as well as estimated Modified Mercalli Intensity (MMI) ranges.

November 7, 2016 M5.0 Cushing, Oklahoma event. According to USGS ShakeMaps [20], the largest PGA recorded during this event was approximately 0.59 g, which was at a hypocentral distance of 5.2 km. Other stations ranging from 6.4 km to 9.6 km from the hypocenter recorded peak PGA values ranging from 0.20 g to 0.32 g [20]. These observed shaking levels are consistent with the estimates from the region-specific ground motion models developed for small to moderate magnitude earthquakes in Oklahoma, Kansas, and Texas. For example, the ground motion models developed by Khosravikia et al. [21] and Zalachoris and Rathje [22] show that, for an earthquake with magnitude of 5.0, the PGA is likely to be larger than 0.2 g at distances less than 10 km from hypocenter, which could go up to 0.6 g at closer distances (i.e. less than 5 km). Combination of this information and fragility curves shown in Fig. 14, suggests that larger magnitude induced earthquakes (M5+) have a significant likelihood (i.e. over 90% for thinner (28ga-min) brick ties and over 70% for code-compliant (22ga-ecc) brick ties) of producing cracking in masonry panel walls nearby the hypocenter (e.g., hypocentral distances less than approximately 5 km).

Fig. 14 also shows the comparison of the fragility curves developed for masonry veneers with Modified Mercalli Intensity (MMI) estimates

Table 3
Coefficients of the ANN equation for estimating top two tie deformations of masonry veneers with respect to PGA.

Brick tie type	Tie	w_1	w_2	b_1	b_2	v_1	v_2	b	$\beta_{D\|IM}$
Code-compliant (22ga-ecc)	d_1	2.30	2.70	0.40	4.34	3.75	1.32	−2.55	0.84
Code-compliant (22ga-ecc)	d_2	2.59	3.18	0.72	5.42	3.88	1.15	−3.19	0.93
Thinner (28ga-min)	d_1	2.07	−3.79	0.17	−4.47	3.70	−2.10	−0.88	0.87
Thinner (28ga-min)	d_2	2.81	−4.95	−0.30	−5.53	3.47	−2.86	−0.91	0.99

from past MMI-to-PGA correlation studies [19]. The qualitative descriptions associated with the MMI values of VI to VIII are given in Table 4. It should be noted that the correlations between Modified Mercalli Intensity and PGA developed by Wald et al. [19] were mainly developed considering ground motions from Western United States. Comparisons of the quantitative damage estimates from the fragility curves with the qualitative damage descriptions of the MMI levels appear to corroborate the damage estimates developed for the masonry veneers in this study. For example, "ordinary" buildings (Table 4) may correspond to residential homes with code-compliant (22ga-ecc) masonry veneers, and "poorly built" structures may correspond to those with non-code compliant (28ga-min) brick ties.

7.1. Scaling factor impact on the fragility assessment of masonry veneers

It is worth noting that selection of region-appropriate ground motions and scaling them for different levels of IM to develop PSDMs is a well-stablished procedure in development of fragility curves. See, for example, the studies done by Choi et al. [55], Nielson and DesRoches [41], Padgett et al. [42], Zakeri et al. [56], Tavares et al. [57], Sichani et al. [58,59], Khosravikia and Clayton [54], among many others. However, it is acknowledged that scaling the ground motions to excessively large scaling factors could add bias to the conclusions. For example, using ground motion recordings from nearby lower magnitude events and scaling those to simulate larger intensities expected by larger magnitude events may not capture the frequency content associated with those larger magnitude events. Thus, care should be taken when scaling ground motions to simulate ground motions of higher intensity.

In a study by Watson-Lamprey and Abrahamson [60], they considered scaling factors ranging from 0.5 to 20, and found that the structural displacement estimates from nonlinear response-history analyses were unbiased for scale factors up to 20. They concluded that "scaling itself does not lead to biased results. This indicates that we can scale by large factors if we select the appropriate recordings." Here, "appropriate recordings" were those representative of the magnitude and distance ranges of interest. In the present study, the ground motions are all taken from those recorded in Oklahoma, Texas, and Kansas since 2008 for earthquakes of magnitude 3.6 to 5.8. In addition, as discussed, the range of spectral accelerations from recorded (unscaled) ground motions are consistent with the spectral accelerations predicted by the USGS one-year hazard maps for induced earthquakes in the considered region.

To investigate the effects of scaling in the present study, the data used to develop the PDSMs in this paper (e.g. the data shown in Fig. 13a) was revisited. Here, all data points from ground motions that were scaled with factors larger than 20 are removed, as it was the largest scaling factor considered by Watson-Lamprey and Abrahamson [60]. Fig. 15a shows the data from ground motion scaling factors less than 20. As seen in the figure, by doing so, fewer data points are considered, particularly in the range of PGAs of 0.8 g and above. However, as seen in the figure, the ANN-based PSDMs developed for both cases (i.e. the model for the randomly selected ground motions and the model where data points from scale factors larger than 20 were removed) are very similar. In addition, Fig. 15b shows the fragility curves developed for masonry veneers with code compliant veneer ties (i.e. 22ecc-ga) considering the analysis corresponding to scaling factors less than 20 as well as the fragility curves presented in Fig. 14 without considering any cap on the scaling factor. As seen in the figure, both fragility curves look very similar; thus, scaling the ground motions to generate higher intensity values does not change the trends in the fragility analysis in this study. Similar trends are also observed for the masonry veneers with thinner (28ga-min) brick ties. It is, however, acknowledged that scaling could have impacts on the conclusions derived from fragility analysis, which is part of the ongoing research of the authors to better understand the impact of scaling on the fragility of masonry veneers.

Table 4
Modified Mercalli Intensity (MMI) damage description.

Damage Level	Description
VI. Strong	Felt by all, many frightened. Some heavy furniture moved; a few instances of fallen plaster. Damage Slight.
VII. Very Strong	Damage negligible in buildings of good design and construction; Slight to moderate in well-built ordinary structures; considerable damage in poorly built or badly designed structure; some chimneys and masonry facades broken.
VIII. Severe	Damage slight in specially designed structures; considerable damage in ordinary substantial buildings with partial collapse; damage great in poorly built structures; falls of chimneys, factory slacks, columns, monuments, walls. Heavy furniture overturned

7.2. Comparison of masonry veneer fragility to induced and New Madrid hazards in Central U.S

Recall that the seismic fragility of different types of structures in Central U.S. have been historically assessed considering New Madrid seismic hazard; see, for example, Nielson and DesRoches [61], Padgett et al. [42], Reneckis and LaFave [32], and Amirihormozaki et al. [62], among others. Often times, these existing fragility functions, claiming to be representative of Central U.S. structures, are applied to broad seismic assessments in Central U.S. regions that are beyond the New Madrid seismic zone. Thus, comparing the differences between the proposed fragility functions based on induced ground motions in this particular region of the Central U.S. (Oklahoma, Texas, and Kansas) and existing fragility functions developed based on assumed New Madrid seismic hazards can highlight potential issues with using existing regional models based on different seismic characteristics.

To investigate how the fragility of masonry veneers subjected to induced earthquake in Central U.S. are different from those subjected to New Madrid seismic hazard, Fig. 16 compares the fragility curves developed in this study with the ones proposed by R&L [27]. The R&L fragility curves were developed using numerical models and nonlinear response history analyses similar to those used in this study; however, the ground motions used in the previous study were representative of the New Madrid seismic hazard, which has historically been used to evaluate seismic vulnerability of structures in the Central United States. As seen in the figure, for a given PGA value, masonry veneers, especially those with thinner brick ties (28ga-min), correspond to a higher probability of cracking and collapse when they are subjected to induced earthquakes compared to the New Madrid seismic hazard. This trend is also observed when the median of the fragility curves is compared. For instance, the median PGA (i.e. the PGA associated with 50% probability of damage) for the cracking damage state of walls with thinner brick ties (28ga-min) is 0.36 g for induced earthquakes, and 0.63 g for the New Madrid seismic hazard. Such differences warn against the use of existing fragility models that claim to be representative of Central U.S. fragility based on assumed seismic hazards (e.g. New Madrid) for induced

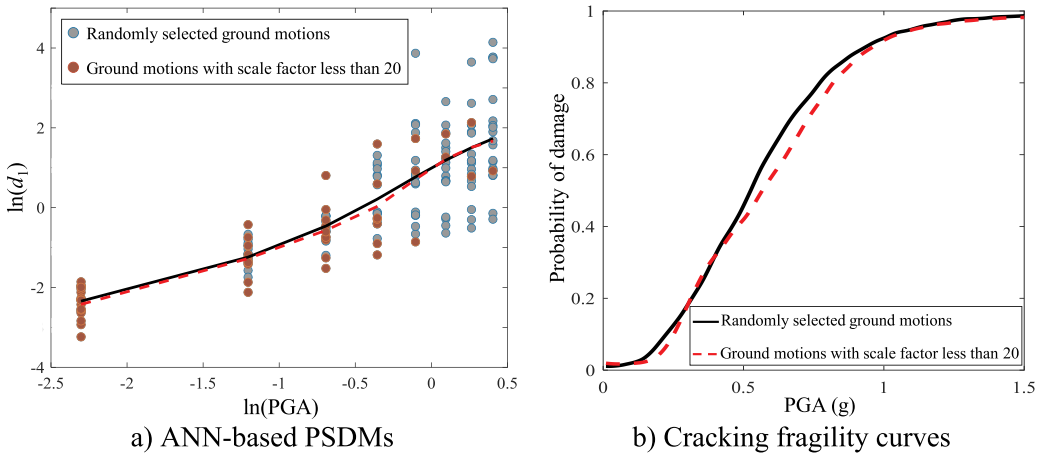

Fig. 15. Comparison of the ANN-based PSDMs for the top tie as well as and cracking fragility curves for masonry veneers with code-compliant ties (22ga-ecc). The solid black curve shows the results for randomly selected motions, and the dashed red curve shows the results for ground motions with scale factor less than 20. (For interpretation of the references to colour in this figure legend, the reader is referred to the Web version of this article.)

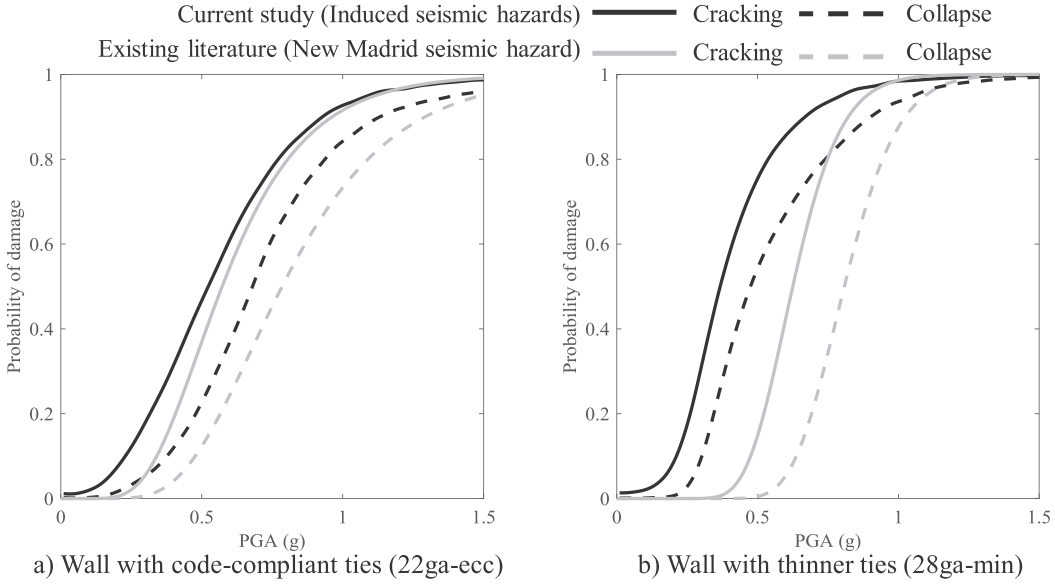

Fig. 16. Comparison of developed fragility curves with existing fragility curves for masonry veneers in Central U.S.

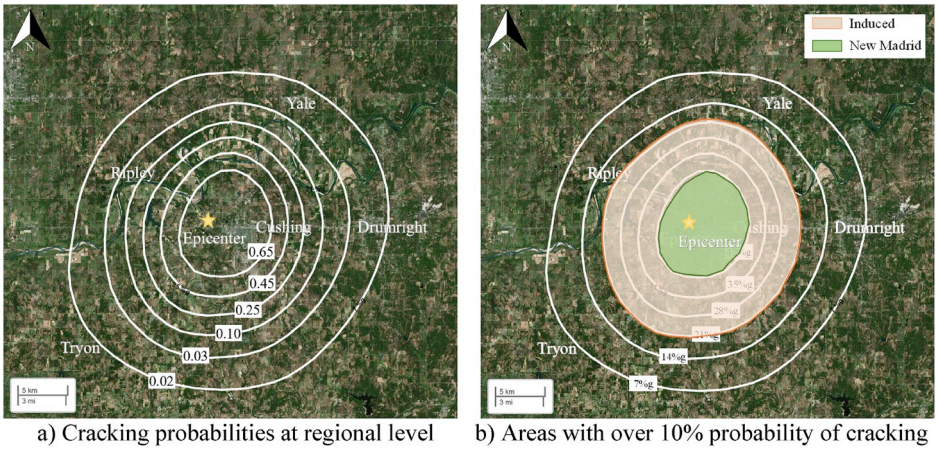

Fig. 17. Regional damage estimates for masonry veneers with thinner (28ga-min) ties based on ground shaking intensities from the November 2016 M5.0 Cushing, OK earthquake.

seismic hazards in the Central U.S.

One potential reason for this observation could be the differences in the spectral shape of the induced ground motions compared to Wen and Wu [25] ground motions, as shown in Fig. 4. Recall that Wen and Wu [25] ground motion set represents the New Madrid seismic hazard, and was used in R&L study for vulnerability evaluation of the masonry veneers. Comparing Fig. 4a and b demonstrates that, within the natural period of the masonry veneers (i.e. 0.165 s–0.265 s), induced earthquakes, on average, have relatively larger values of spectral accelerations than Wen and Wu ground motions when normalized to the same PGA value. However, such differences in the fragility of masonry veneers to induced and New Madrid seismic hazards in Central U.S. raises questions like: Why do induced earthquakes tend to provide higher likelihood of damage for a given PGA level compared to the New Madrid seismic hazard that generally contains larger magnitude earthquakes? Which characteristics of the ground motions cause this difference in vulnerability? Are similar conclusions observed for fragility curves developed with respect to other IMs? Are these differences because of the slight differences in the modeling approaches between the present and R&L studies? Such questions related to the cause of these differences are beyond the scope of this paper and necessitate further research to be fully addressed. These topics are the focus of ongoing studies by the authors.

8. Regional impacts of the induced earthquakes

The aforementioned fragility curves can be combined with PGA contours from previous events to estimate the regional impacts of induced earthquakes with respect to masonry veneer damage in residential construction. For the purpose of demonstration, the PGA contours for the November 7, 2016 M5.0 Cushing, Oklahoma event are derived from the ShakeMaps [20] provided on the USGS website [63]. Fig. 17a shows contours for the probability of cracking damage in veneers walls with thinner (28ga-min) ties. According to this figure, an area of over 1372 km^2 around the epicenter is estimated to have over 10% probability of cracking for this type of veneer. In this regard, Fig. 17b compares the regional damage estimates resulting from the fragility curves developed in this study (i.e. based on induced seismic hazards) and existing fragility curves in the literature for Central United States (i.e. based on New Madrid seismic hazards). In this figure, the areas with over 10% likelihood of cracking predicted from the different fragility curves are shaded. As seen, the higher likelihood of damage for a given PGA predicted from fragility curves developed using induced earthquake motions results in larger estimates of affected area compared to the predictions using existing fragility curves based on New Madrid seismic hazards. In fact, the area with over 10% probability of cracking based on induced earthquake fragilities (i.e. 1372 km^2) is almost four times larger than the area expecting the same likelihood of damage using existing fragility curves based on New Madrid hazards (i.e. 346 km^2). These results demonstrate the importance of using fragilities curves developed for the particular seismic hazards of interest when conducting regional loss estimates. In this particular case, if existing fragility curves for the Central U.S., many of which were developed assuming New Madrid seismic hazards, were broadly applied to loss predictions for induced earthquake events in the Central U.S., the extent of damage could be significantly underestimated.

9. Summary and conclusion

The recent seismic activities in Central U.S. have resulted in millions of dollars of damage, primarily to residential buildings including chimneys and masonry veneers. Most of these earthquakes are believed to be human-induced earthquakes associated with more intense natural gas and petroleum productions starting 2009. This study employs a probabilistic framework to better understand and evaluate the impacts of such earthquakes on masonry veneers in that region. The proposed framework utilizes a suite of 200 ground motions from 36 seismic events with magnitude of 3.6–5.8 that have been classified as human-induced earthquakes in that region. In the framework, experimentally-validated computational models are developed to simulate the seismic performance of non-seismically detailed brick veneers. The proposed framework adopts an Artificial Neural Network (ANN) to developed probabilistic seismic demand models (PSDMs). It is shown that using ANN instead of the conventional method of linear regression leads to more accurate PSDMs, and thereby more reliable performance predictions. The main findings of this study are as follows:

- For induced earthquakes, PGA levels of approximately 0.52 g result in 50% probability of cracking in brick veneers with code-complaint (22ga-ecc) brick ties. For those with thinner brick ties (28ga-min) that are commonly used in residential construction, a lower PGA of 0.36 g results in 50% likelihood of cracking.
- The masonry veneer fragility curves for induced earthquakes in Central U.S. are in line what is expected from Modified Mercalli Intensity (MMI) descriptions and MMI-to-PGA correlations.
- For a given PGA, induced earthquakes are more likely to cause cracking and collapse for masonry veneers, especially those with thinner brick ties (22ga-ecc), compared to what is expected using existing fragility functions based on New Madrid seismic hazards.
- When used in regional damage estimates, the affected areas predicted by fragilities based on induced seismic hazards could be significantly larger than what is predicted using existing Central U.S. fragility curves developed for New Madrid seismic hazards.

It should be noted the findings of this study are only limited to non-seismically detailed masonry veneers, and more study should be conducted to fully understand the impacts of induced earthquakes on different types of infrastructure.

Declaration of competing interest

We wish to confirm that there are no known conflicts of interest associated with this publication and there has been no significant financial support for this work that could have influenced its outcome.

CRediT authorship contribution statement

Farid Khosravikia: Conceptualization, Formal analysis, Writing - original draft. **Jennifer Kurkowski:** Conceptualization, Formal analysis, Writing - original draft. **Patricia Clayton:** Conceptualization, Formal analysis, Writing - original draft.

Acknowledgements

This work was financially supported by the State of Texas through the TexNet Seismic Monitoring Project and the Industrial Associates of the Center for Integrated Seismic Research (CISR) at the Bureau of Economic Geology of the University of Texas. The opinions and findings expressed herein are those of the authors and not the sponsors.

Appendix A. Supplementary data

Supplementary data to this article can be found online at https://doi.org/10.1016/j.jobe.2019.101100.

References

[1] M. Petersen, C.S. Mueller, M.P. Moschetti, S.M. Hoover, A.L. Llenos, W. L. Ellsworth, et al., One-Year Seismic Hazard Forecast for the Central and Eastern United States from Induced and Natural Earthquakes, Open-File Report 2016, 2016.

[2] C. Frohlich, H. Deshon, B. Stump, C. Hayward, M. Hornbach, J.I. Walter, A historical review of induced earthquakes in Texas, Seismol. Res. Lett. 87 (2016) 1–17, https://doi.org/10.1785/0220160016.
[3] M.J. Hornbach, M. Jones, M. Scales, H.R. DeShon, M.B. Magnani, C. Frohlich, et al., Ellenburger wastewater injection and seismicity in North Texas, Phys. Earth Planet. Inter. 261 (2016) 54–68.
[4] S.E. Hough, Shaking from injection-induced earthquakes in the central and eastern United States, Bull. Seismol. Soc. Am. 104 (5) (2014) 2619–2626.
[5] C. Frohlich, W. Ellsworth, W.A. Brown, M. Brunt, J. Luetgert, T. MacDonald, et al., The 17 May 2012 M4. 8 earthquake near Timpson, East Texas: an event possibly triggered by fluid injection, J. Geophys. Res.: Solid Earth 119 (2014) 581–593.
[6] W.L. Ellsworth, Injection-induced earthquakes, Science 341 (2013) 1225942.
[7] M. Weingarten, S. Ge, J.W. Godt, B.A. Bekins, J.L. Rubinstein, High-rate injection is associated with the increase in US mid-continent seismicity, Science 348 (2015) 1336–1340.
[8] M.D. Petersen, C.S. Mueller, M.P. Moschetti, S.M. Hoover, A.M. Shumway, D. E. McNamara, et al., 2017 one-year seismic-hazard forecast for the Central and Eastern United States from induced and natural earthquakes, Seismol. Res. Lett. 88 (2017) 772–783.
[9] S. Barrett, The Link between Hydrofracking, Wastewater Injection and Earthquakes: Key Issues for Re/insurers, Swiss Reinsurance Company, 2016.
[10] C. Jones, C. Killman, Earthquake Insurance: 3 in 20 Claims Approved in Oklahoma since 2010, Tulsa World News, 2017.
[11] E.E.R.I. Oklahoma, USA Earthquake Clearinghouse. http://www.eqclearinghouse.org/2016-09-03-oklahoma, 2016.
[12] Time, n.d.:Retrieved in August 2019, https://time.com/2890114/oklahoma-Earthquake-Fracking-Insurance.
[13] R.E. Chase, A.B. Liel, Potential for Damage to Brittle Structures in Induced Earthquakes, World Conference in Earthquake Engineering, Santiago Chile, 2017.
[14] R.E. Chase, Structural Response and Risk Considering Regional Ground Motion Characteristics, 2018.
[15] J.P. Bradtmueller, S.P. Foley, Historical trends of exterior wall materials used in US residential construction, in: 50th ASC Annual International Conference Proceedings, 2014.
[16] G.E. Hinton, Connectionist learning procedures, Artif. Intell. 40 (1989) 185–234, https://doi.org/10.1016/0004–3702(89)90049–0.
[17] T. Hastie, R. Tibshirani, J. Friedman, The Elements of Statistical Learning, Springer Series in Statistics Springer, 2009, https://doi.org/10.1007/978–0–387–84858–7.
[18] I. Goodfellow, Y. Bengio, A. Courville, Deep Learning. Adaptive Computation and Machine Learning Series, MIT Press, 2016.
[19] D.J. Wald, V. Quitoriano, T.H. Heaton, H. Kanamori, Relationships between peak ground acceleration, peak ground velocity, and modified Mercalli intensity in California, Earthq. Spectra 15 (1999) 557–564.
[20] D.J. Wald, B.C. Worden, V. Quitoriano, K.L. Pankow, ShakeMap® Manual. Technical Manual, Users Guide, and Software Guide Version, 2006.
[21] F. Khosravikia, P. Clayton, Z. Nagy, Artificial neural network based framework for developing ground motion models for natural and induced earthquakes in Texas, Oklahoma, and Kansas, Seismol. Res. Lett. 90 (2A) (2018) 604–613.
[22] G. Zalachoris, E.M. Rathje, Ground motion model for small-to-moderate earthquakes in Texas, Oklahoma, and Kansas, Earthq. Spectra 35 (2019) 1–20.
[23] F. Khosravikia, A. Potter, V. Prakhov, G. Zalachoris, T. Cheng, A. Tiwari, et al., Seismic Vulnerability and Post-Event Actions for Texas Bridge Infrastructure, Center for Transportation Research (CTR), 2018. FHWA/TX-18/0-6916-1.
[24] F. Khosravikia, Y. Zeinali, Z. Nagy, P. Clayton, E. Rathje, Neural Network-Based Equations for Predicting PGA and PGV in Texas, Oklahoma, and Kansas, Geotechnical Earthquake Engineering and Soil Dynamics V, 2018, https://doi.org/10.1061/9780784481462.052. Austin, TX, USA.
[25] Y.K. Wen, C.-L. Wu, Uniform hazard ground motions for mid-America cities, Earthq. Spectra 17 (2001) 359–384.
[26] F. McKenna, G.L. Fenves, M.H. Scott, others, Open System for Earthquake Engineering Simulation, University of California, Berkeley, CA, 2000.
[27] D. Reneckis, J.M. LaFave, Seismic Performance of Anchored Brick Veneer, Newmark Structural Engineering Laboratory. University of Illinois at Urbana-Champaign, 2009. Report No. NSEL-016.
[28] Masonry Standards Joint Committee, Building Code Requirements and Specification for Masonry Structures, TMS 402/ACI 530/ASCE 5, The Masonry Society, American Concrete Institute, and American Society of Civil Engineers, Boulder, CO, Farmington Hills, MI, and Reston, VA, USA, 2013. Masonry Society.
[29] H.O. Okail, P.B. Shing, R.E. Klingner, W.M. McGinley, Performance of clay masonry veneer in wood-stud walls subjected to out-of-plane seismic loads, Earthq. Eng. Struct. Dyn. 39 (2010) 1585–1609.
[30] H.O. Okail, P.B. Shing, W.M. McGinley, R.E. Klingner, S. Jo, D.I. McLean, Shaking-table tests of a full-scale single-story masonry veneer wood-frame structure, Earthq. Eng. Struct. Dyn. 40 (2011) 509–530.
[31] R.E. Klingner, W.M. McGinley, P.B. Shing, D.I. McLean, S. Jo, H. Okail, Seismic performance of low-rise wood-framed and reinforced masonry buildings with clay masonry veneer, J. Struct. Eng. 139 (2013) 1326–1339.
[32] D. Reneckis, J.M. LaFave, Out-of-plane seismic performance and detailing of brick veneer walls, J. Struct. Eng. 136 (2010) 781–794.
[33] A.W. Page, Newcastle earthquake-behaviour of masonry structures, Mason. Int. 5 (1991) 11–18.
[34] D. Reneckis, J.M. LaFave, Analysis of brick veneer walls on wood frame construction subjected to out-of-plane loads, Constr. Build. Mater. 19 (2005) 430–447.
[35] D. Reneckis, J.M. LaFave, Out-of-plane seismic performance and fragility analysis of anchored brick veneer, Struct. Saf. 35 (2012) 1–17.
[36] J.M. LaFave, Z. Gao, D.E. Holder, M.J. Kuo, L.A. Fahnestock, Commercial and residential building performance during the may 20, 2013, tornado in Moore, Oklahoma, J. Perform. Constr. Facil. 30 (2014) 4014210.
[37] NDS, National Design Specification for Wood Construction. American Forest and Paper Association, American Forest & Paper Association, Washington, D.C., 2001.
[38] K. Doherty, M.C. Griffith, N. Lam, J. Wilson, Displacement-based seismic analysis for out-of-plane bending of unreinforced masonry walls, Earthq. Eng. Struct. Dyn. 31 (2002) 833–850.
[39] C.C. Simsir, Influence of Diaphragm Flexibility on the Out-Of-Plane Dynamic Response of Unreinforced Masonry Walls, University of Illinois at Urbana-Champaign, 2004.
[40] C.A. Cornell, F. Jalayer, R.O. Hamburger, D.A. Foutch, Probabilistic basis for 2000 SAC federal emergency management agency steel moment frame guidelines, J. Struct. Eng. 128 (2002) 526–533.
[41] B.G. Nielson, R. DesRoches, Analytical seismic fragility curves for typical bridges in the central and southeastern United States, Earthq. Spectra 23 (2007) 615–633.
[42] J.E. Padgett, B.G. Nielson, R. Desroches, Selection of optimal intensity measures in probabilistic seismic demand models of highway bridge portfolios, Earthq. Eng. Struct. Dyn. 37 (2008) 711–725.
[43] W.S. McCulloch, W. Pitts, A logical calculus of the ideas immanent in nervous activity, Bull. Math. Biophys. 5 (1943) 115–133.
[44] G. Cybenko, Approximation by superpositions of a sigmoidal function, Math. Control, Signals, Syst. 5 (4) (1992), https://doi.org/10.1007/BF02551274, 455–455.
[45] B. Karlik, A.V. Olgac, Performance analysis of various activation functions in generalized MLP architectures of neural networks, Int. J. Artif. Intell. Expert Syst. 1 (2011) 111–122.
[46] L.I. Perlovsky, Neural Networks and Intellect: Using Model-Based Concepts, Oxford University Press, New York, 2001.
[47] D.W. Marquardt, An algorithm for least-squares estimation of nonlinear parameters, J. Soc. Ind. Appl. Math. 11 (1963) 431–441.
[48] F.D. Foresee, M.T. Hagan, Gauss-Newton approximation to Bayesian learning, in: Proceedings of the 1997 International Joint Conference on Neural Networks, vol. 3, 1997, pp. 1930–1935.
[49] A.H. Alavi, A.H. Gandomi, Prediction of principal ground-motion parameters using a hybrid method coupling artificial neural networks and simulated annealing, Comput. Struct. 89 (2011) 2176–2194, https://doi.org/10.1016/j.compstruc.2011.08.019.
[50] C. Liu, M. White, G. Newell, Measuring and comparing the accuracy of species distribution models with presence–absence data, Ecography 34 (2011) 232–243.
[51] A.H. Gandomi, A.H. Alavi, M. Mousavi, S.M. Tabatabaei, A hybrid computational approach to derive new ground-motion prediction equations, Eng. Appl. Artif. Intell. 24 (2011) 717–732, https://doi.org/10.1016/j.engappai.2011.01.005.
[52] M. Tokunaga, M. Nishikawa, A. Matsumoto, S. Nanbu, A. Nakagawa, Y. Maeda, et al., The relationship between measured values and values predicted using multiple regression analysis for mean motor FIM at discharge, Jpn. J. Compr. Rehabil. Sci. 6 (2015) 86–90.
[53] M. Gandomi, M. Soltanpour, M.R. Zolfaghari, A.H. Gandomi, Prediction of peak ground acceleration of Iran' s tectonic regions using a hybrid soft computing technique, Geosci. Front. 7 (2016) 75–82, https://doi.org/10.1016/j.gsf.2014.10.004.
[54] F. Khosravikia, P. Clayton, Updated evaluation metrics for optimal intensity measure selection in probabilistic seismic demand models, Eng. Struct. 202 (2020), 109899, https://doi.org/10.1016/j.engstruct.2019.109899.
[55] E. Choi, R. DesRoches, B. Nielson, Seismic fragility of typical bridges in moderate seismic zones, Eng. Struct. 26 (2004) 187–199.
[56] B. Zakeri, J.E. Padgett, G. Ghodrati Amiri, Fragility assessment for seismically retrofitted skewed reinforced concrete box girder bridges, J. Perform. Constr. Facil. 29 (2013), 4014043.
[57] D.H. Tavares, J.R. Suescun, P. Paultre, J.E. Padgett, Seismic fragility of a highway bridge in Quebec, J. Bridge Eng. 18 (2013) 1131–1139, https://doi.org/10.1061/(ASCE)BE.1943-5592.0000471.
[58] M.E. Sichani, J.E. Padgett, V. Bisadi, Probabilistic seismic analysis of concrete dry cask structures, Struct. Saf. 73 (2018) 87–98.
[59] M.E. Sichani, M. Hanifehzadeh, J.E. Padgett, B. Gencturk, Probabilistic analysis of vertical concrete dry casks subjected to tip-over and aging effects, Nucl. Eng. Des. 343 (2019) 232–247.
[60] J. Watson-Lamprey, N. Abrahamson, Selection of ground motion time series and limits on scaling, Soil Dyn. Earthq. Eng. 26 (2006) 477–482.
[61] B.G. Nielson, R. DesRoches, Seismic fragility methodology for highway bridges using a component level approach, Earthq. Eng. Struct. Dyn. 36 (2007) 823–839.
[62] E. Amirihormozaki, G. Pekcan, A. Itani, Analytical modeling of horizontally curved steel girder highway bridges for seismic analysis, J. Earthq. Eng. 19 (2015), https://doi.org/10.1080/13632469.2014.962667.
[63] USGS. https://earthquake.usgs.gov/earthquakes/eventpage/us100075y8/map, 2016.